

Development of a non-delay line constant fraction discriminator based on the Padé approximant for time-of-flight positron emission tomography scanners

This content has been downloaded from IOPscience. Please scroll down to see the full text.

2015 JINST 10 P01005

(<http://iopscience.iop.org/1748-0221/10/01/P01005>)

View [the table of contents for this issue](#), or go to the [journal homepage](#) for more

Download details:

This content was downloaded by: jaes

IP Address: 171.66.219.134

This content was downloaded on 16/01/2015 at 17:21

Please note that [terms and conditions apply](#).

Development of a non-delay line constant fraction discriminator based on the Padé approximant for time-of-flight positron emission tomography scanners

S.Y. Kim,^{a,1} G.B. Ko,^{a,b,1} S.I. Kwon^a and J.S. Lee^{a,b,c,2}

^aDepartment of Nuclear Medicine, Seoul National University College of Medicine,
103 Daehak-ro, Jongno-gu, Seoul 110-799, Korea

^bDepartment of Biomedical Sciences, Seoul National University College of Medicine,
103 Daehak-ro, Jongno-gu, Seoul 110-799, Korea

^cInstitute of Radiation Medicine, Medical Research Center, Seoul National University College of Medicine,
103 Daehak-ro, Jongno-gu, Seoul 110-799, Korea

E-mail: jaes@snu.ac.kr

ABSTRACT: In positron emission tomography, the constant fraction discriminator (CFD) circuit is used to acquire accurate arrival times for the annihilation photons with minimum sensitivity to time walk. As the number of readout channels increases, it becomes difficult to use conventional CFDs because of the large amount of space required for the delay line part of the circuit. To make the CFD compact, flexible, and easily controllable, a non-delay-line CFD based on the Padé approximant is proposed. The non-delay-line CFD developed in this study is shown to have timing performance that is similar to that of a conventional delay-line-based CFD in terms of the coincidence resolving time of a fast photomultiplier tube detector. This CFD can easily be applied to various positron emission tomography system designs that contain high-density detectors with multi-channel structures.

KEYWORDS: Analogue electronic circuits; Gamma camera, SPECT, PET PET/CT, coronary CT angiography (CTA); Front-end electronics for detector readout

¹Co-first authors.

²Corresponding author.

Contents

1	Introduction	1
2	Materials and methods	2
2.1	Padé approximant of the ideal delay line	2
2.2	Circuit simulation of the Padé approximant	3
2.3	Implementation of the NDL CFD	3
2.4	Calibration of the NDL CFD	4
2.5	Experimental setup for evaluation of time resolution	4
3	Results	5
3.1	Circuit simulation of the delay line	5
3.2	CFD and delay-line behavior	7
3.3	Timing measurement of the TOF detector	8
4	Discussion	9
5	Conclusion	10

1 Introduction

Time measurement of radiation events is essential in various fields, including nuclear and particle physics, mass spectrometry, and medical imaging [1–5]. For example, in medical imaging, precise measurement of the difference between the arrival times of mutually annihilated gamma-ray photons in positron emission tomography (PET), which is a major functional and molecular medical imaging modality, has several benefits. The incorporation of this so-called time-of-flight (TOF) information into the image reconstruction procedure reduces noise, enhances contrast, and improves diagnostic accuracy [6–10].

The standard method used to measure the arrival time difference in PET uses a time-to-digital converter (TDC), which receives digital input pulses with a fast rise time and a specific voltage level. Accurate generation of digital pulses from the analog signals of the PET scintillation detectors with their relatively slow rise times is therefore a critical procedure. The two main electronic circuits that are used to generate digital pulses from the scintillation detectors are the leading edge discriminator (LED) [11] and the constant fraction discriminator (CFD) [12]. Implementation of the LED is relatively easy, because the LED generates the trigger signal at a specific voltage threshold using a comparator. However, while LEDs with very low trigger thresholds yield good timing resolution in PET detectors [6, 13, 14], many unwanted events (e.g., electrical noise and scattering events) triggered by the low threshold can result in dead time for the subsequent electronics and loss of information.

The CFD is superior to the LED for scintillation detector applications because it does not cause time walk errors, i.e., the timing variation generated because of the dependency of the trigger time on the input pulse amplitude [15, 16]. However, the main drawbacks of the CFD are the relatively high complexity of implementing the electronic circuitry and the large amount of space required for circuit implementation. As we will describe in detail later, one of the main components of the CFD is an analog delay. The long transmission lines that are conventionally used to delay the analog signal require a large amount space and prevent concise setting of the delay time. Delay techniques that do not use a massive delay line have mainly been proposed for on-chip applications [17, 18]. These previous approaches used simple analog filters, dedicated delay lines or amplifier chains to delay the signals.

This study develops an accurate non-delay-line (NDL) CFD using an analog filter for modern TOF PET applications. The delay line transfer function was modeled using the Padé approximant to the transfer function of an ideal delay line to improve the time delay accuracy. The NDL CFD developed in this study has several advantages, including outstanding space reduction, easy impedance matching of the signal transmission, and flexible control of the delay line. In this study, we evaluate the timing performance of the developed CFD using a pair of scintillation detector modules made from lutetium-yttrium oxyorthosilicate (LYSO) crystal and a fast photomultiplier tube (PMT).

2 Materials and methods

2.1 Padé approximant of the ideal delay line

The transfer function of the ideal delay, $H(s)$, is the Laplace transform of the delayed signal:

$$x(t - \tau) = x(t) \otimes h(t) \xleftrightarrow{L} X(s)H(s) = X(s)e^{-\tau s}. \quad (2.1)$$

$$H(s) = e^{-\tau s}. \quad (2.2)$$

This transfer function can be approximated by the Padé approximant as a rational function of a given order [19, 20]. The general form of the n -th-order Padé approximant is

$$H(s) = e^{-\tau s} \approx \frac{1 - k_1 s + k_2 s^2 - \dots + (-1)^n k_n s^n}{1 + k_1 s + k_2 s^2 + \dots + k_n s^n}. \quad (2.3)$$

This rational function can be implemented as an electrical circuit in the form of a general n -th-order all-pass filter with numerator and denominator polynomials of the same degree. For this class of Padé approximant, convergence with respect to the L_∞ and L_2 norms is guaranteed for the frequency response [21]. In the simplest form of the filter, the first-order approximation coefficients are defined as $k_1 = \tau/2$ and the other coefficients are defined as $k_i = 0$, as shown below in equation (2.4). Figure 1(a) shows the all-pass filter circuit, which was implemented using only one operational amplifier (op-amp) based on the first-order approximation with $\tau = 2R_d C_d$. While this circuit requires the minimum number of electric components, it may also have a non-minimum phase-shift artifact. The transfer function of the circuit is

$$H(s) = \frac{1 - \left(\frac{\tau}{2}\right)s}{1 + \left(\frac{\tau}{2}\right)s} = \frac{1 - \frac{2R_d C_d}{2}s}{1 + \frac{2R_d C_d}{2}s}. \quad (2.4)$$

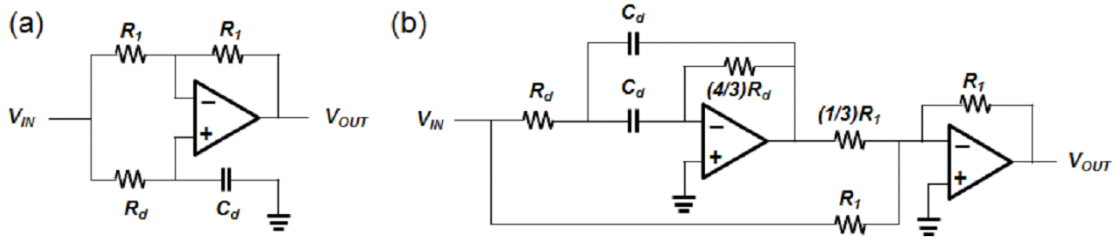


Figure 1. (a) First-order and (b) second-order implementations of the delay circuits based on the Padé approximant.

The second-order approximation, which is more accurate but also more complex, can be given as

$$H(s) = \frac{1 - \left(\frac{\tau}{2}\right)s + \left(\frac{\tau^2}{12}\right)s^2}{1 + \left(\frac{\tau}{2}\right)s + \left(\frac{\tau^2}{12}\right)s^2} = \frac{1 - \frac{4R_d C_d}{2}s + \frac{(4R_d C_d)^2}{12}s^2}{1 + \frac{4R_d C_d}{2}s + \frac{(4R_d C_d)^2}{12}s^2}. \quad (2.5)$$

The electrical circuit implementation for this approximation with $\tau = 4R_d C_d$ is shown in figure 1(b). The additional pole-zero pair generated by the increased order of the all-pass filter leads to an increase in the total phase shift at the center frequency. The center frequency can also be increased when the filter is implemented with the same group delay. Thus, the second-order implementation with two poles and two zeros would yield a less distorted output in terms of overshoot and faster signal convergence than the first-order implementation with only one pole and one zero.

2.2 Circuit simulation of the Padé approximant

We performed an electrical circuit simulation to compare the properties of the first-order and second-order approximation circuits for the PET CFD. The input analog pulse signal used for the simulation was obtained from the LYSO-PMT detector using a digital oscilloscope (DSO9064A; Agilent, San Jose, CA, U.S.A.), with a 10 GHz sampling rate and a 600 MHz bandwidth. In all simulations, the value of the delay capacitor (C_d) was fixed at 5 pF. The delay resistor (R_d) of both the first-order and second-order circuits was varied from 0.2 to 2.0 k Ω in steps of 0.2 k Ω and from 0.1 to 10 k Ω in steps of 0.1 k Ω to yield a delay of 2–20 ns in steps of 2 ns. Distortion of the overall signal shape and a ripple in the delayed signal were observed. The differences between the set ($2R_d C_d$ for the first-order approximation and $4R_d C_d$ for the second-order approximation) and measured delays were also investigated. The delay was defined as the time difference between the original signal and the delayed signal at 70% of the maximum amplitude of the original signal.

2.3 Implementation of the NDLCFD

From the results of the delay circuit simulations, we conclude that the first-order delay circuit is sufficient for the PET CFD (see section 3.1 for more details). The CFD module was therefore implemented using the first-order delay circuit shown in figure 1(a). For implementation of the variable delay lines, C_d was fixed to 4.7 pF, and R_d was selected using a dip switch from values of 24, 51, 100, 150, 200, 240, 300, and 330 Ω to yield delays of 0.23, 0.48, 0.94, 1.41, 1.88, 2.26, 2.82, and 3.10 ns, respectively.

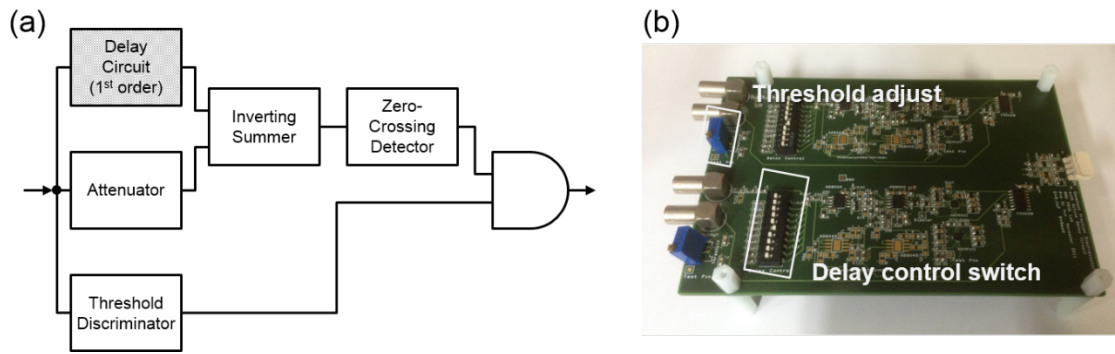


Figure 2. (a) Block diagram of the developed NDL CFD, and (b) CFD module comprising a PCB circuit.

A block diagram of the CFD module is shown in figure 2(a). The input pulse was split into three paths: signal delay, attenuation, and threshold discriminator. The delayed signal and the attenuated signal were summed through the inverting summing amplifier to generate a bipolar signal. A zero-crossing detector then detected the zero-crossing point of the bipolar signal and generated a digital pulse at a constant trigger point regardless of the signal amplitude. The threshold discriminator generated a digital pulse only when the input signal amplitude exceeded a threshold voltage to reject low-level noise and avoid un-wanted trigger. The output digital pulse was produced from the logical AND of the zero-crossing detector and threshold discriminator signals. The attenuation circuit was implemented using a simple voltage divider circuit, and the attenuation constant was set to either 0.2 or 0.4.

Figure 2(b) shows the implemented CFD module as described above. The threshold voltage level can be controlled by altering the value of the variable resistor, and the delay value can be selected using the dip switch.

2.4 Calibration of the NDL CFD

The real delay may not be exactly the same as the desired delay value that was calculated from the R_d and C_d values because of the internal propagation time of the op-amp, the routing length of the printed circuit board (PCB) lines, and the phase distortion of the pulse. Therefore, the delay must be measured and calibrated to guarantee the accuracy of the experiments. All measurements were performed with a 350-MHz, 2.5-GS/s digital oscilloscope (MSO4034; Tektronix, Beaverton, OR, U.S.A.), while calculating the timing difference of 100 averaged, delayed and attenuated pulses at the input pins of the inverting summer (see figure 2(a)) at 50% of the maximum signal amplitude. The measured delay values are used throughout the analysis of the experimental results in this paper.

2.5 Experimental setup for evaluation of time resolution

To assess the feasibility of the NDL CFD for use in TOF PET applications, the coincidence resolving time (CRT) of the fast PMT detectors with the NDL CFDs was measured and compared with that of the conventional delay-line CFDs (DL CFDs).

A block diagram of the data acquisition setup used for the energy and timing measurements is shown in figure 3. The experimental setup consisted of commercial nuclear instrumentation mod-

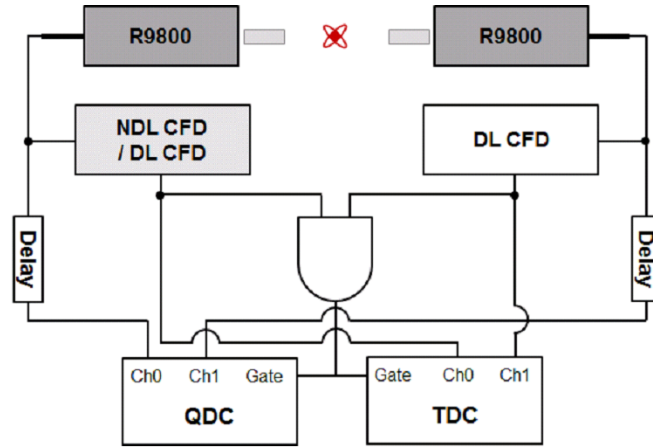


Figure 3. Experimental setup for CRT measurement of the PMT.

ules (NIMs) and CFD circuits. Two fast PMTs (R9800; Hamamatsu Photonics K.K., Hamamatsu, Japan) coupled with LYSO crystals ($4 \times 4 \times 10 \text{ mm}^3$) were used in the evaluation [21]. One of the PMT signals was fed into the conventional DL CFD (the “reference CFD”) and the other signal was fed into the NDL CFD or DL CFD (the “target CFD”) for comparison. In the evaluation of CFD performance, various time delays (from 0.5 ns to 4 ns at eight uneven intervals) and attenuation constants of 0.2 and 0.4 were applied for the target NDL and DL CFDs. The thresholds of both CFD were fixed to 50 mV. For the reference CFD, the delay and the attenuation were fixed at 1 ns and 20%, respectively. For the DL CFD, we used eight transmission lines (RG 174/U coaxial cables; 101.05 pF/m nominal capacitance and 50Ω nominal impedance) of different lengths to yield various delays. The delays of each transmission line were also measured accurately using the oscilloscope. The signal outputs from the CFDs were then fed into a coincidence logic unit (N455, CAEN SpA, Viareggio, Italy) executing in the AND mode. The output coincidence trigger signal was used as STOP/GATE signals for the TDC (V775N, CAEN) and the charge-to-digital converter (QDC; V965, CAEN). All measurements were performed using a ^{22}Na gamma-ray source and 50,000 coincidence events were acquired under each condition [22, 23].

3 Results

3.1 Circuit simulation of the delay line

The first-order and second-order delay circuits have the same group delays at low frequencies but have different frequency responses, as shown in figure 4. The center frequency of the second-order circuit is higher than that of the first-order circuit, which implies that the second-order circuit delays the scintillation pulses more accurately than the first-order circuit.

The delayed pulses, which were simulated using a pulse captured from the scintillation detector, are shown in figure 5, where we have zoomed in on the rising edges of the pulses. The 180° phase shift of the second-order filter is corrected in the figure for convenience of appearance and analysis. The time domain ripple and the slope degradation are larger for the first order delay

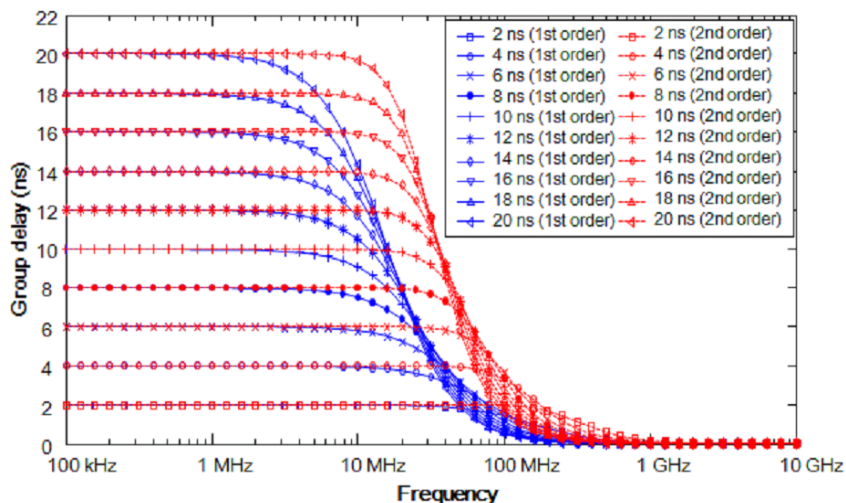


Figure 4. Group delay dependency on frequency of the first-order and second-order delay circuits. The solid blue lines indicate results for the first-order circuit and the dashed red lines indicate results for the second-order circuit.

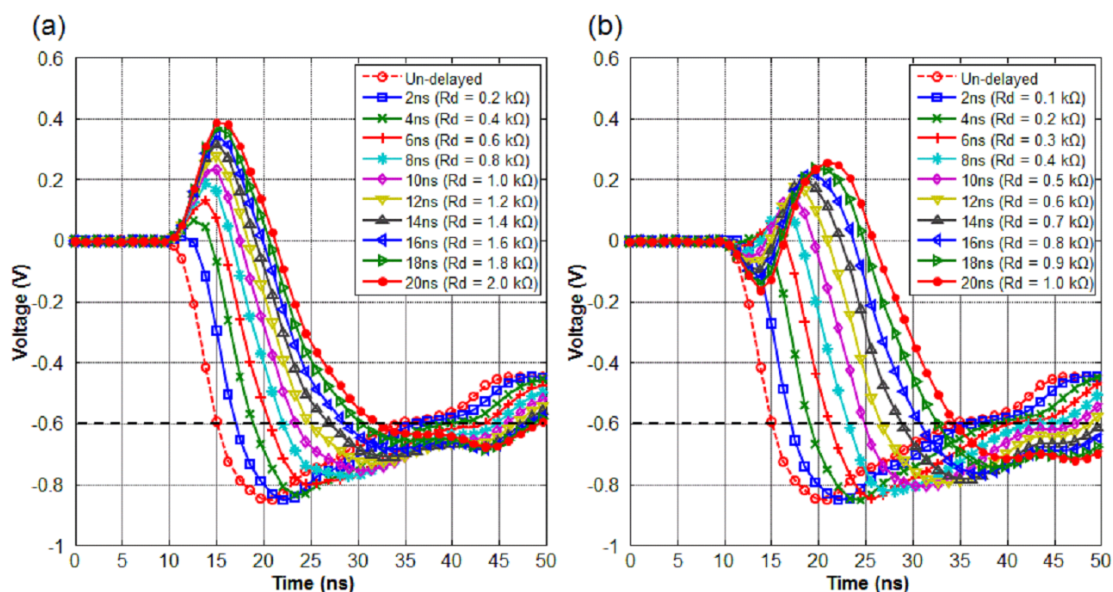


Figure 5. Simulation results for (a) first-order and (b) second-order Padé approximants. The 180° phase shift of the second-order filter was corrected in the figure for appearance and analysis.

circuit than for the second order circuit. They are particularly severe for larger delays, because the center frequency of each all-pass filter decreases with increasing delay, as shown in figure 4.

Figure 6 presents the difference between the delays that were calculated from resistor and capacitor values (calculated delay) and delays from the circuit simulations (simulated delay). Although the group delays of the delay circuits at low frequencies are the same as the calculated delays, the simulated delays differ from the calculated delays, particularly for the first-order filter,

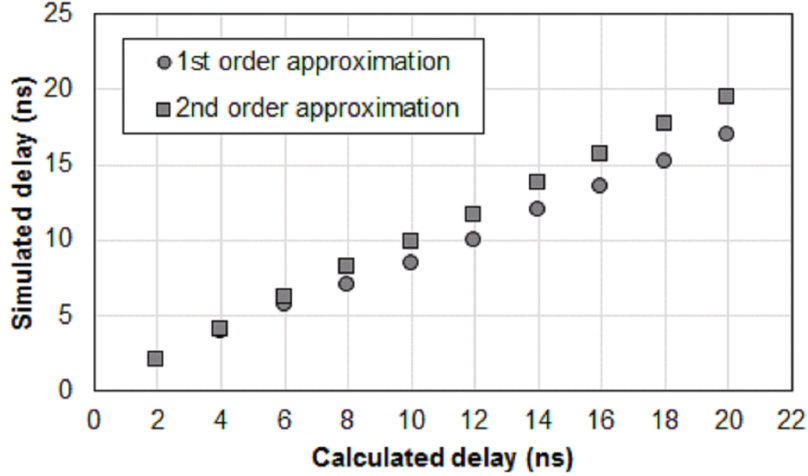


Figure 6. Time difference between the delay calculated using the RC values (calculated delay) and the delay from the simulation results (simulated delay). Circles denote the results for the first-order circuit and squares denote the results for the second-order circuit.

because of the bandwidth limitations, as mentioned earlier. The differences between the simulated delays and the calculated delays of the first- and second-order filters are less than 5% for delays of up to 6 and 20 ns, respectively.

Although the overall performance of the second-order circuit is better than that of the first-order circuit, we conclude that the first-order circuit is sufficient for our purposes because the CFDs used in TOF PET typically use a delay of only a few nanoseconds. The CFD delay time should be equal to or less than the input pulse rise time and the suggested delay time is determined by following the rule of thumb below [22].

$$\text{delay time} = \text{rise time} \times (1 - \text{CFD fraction}), \quad (3.1)$$

where the *CFD fraction* indicates the amount of signal attenuation by the attenuator.

In the simulation, the rise time of the undelayed pulse was ~ 5 ns. Therefore, for CFD fractions of 0.2 and 0.4, the optimal delays suggested by the rule of thumb are only 4 and 3 ns, respectively. In fact, the scintillation pulse rise time is closely related to the timing resolution of the scintillation detector. Modern scintillation detectors used in TOF applications have rise times of less than 5 ns [22, 24], and thus the 4 ns range is sufficient for this purpose. At delays of less than 4 ns, the first-order delay circuit yields a peak-to-peak ripple of less than 8% and a delayed time difference of 3%.

3.2 CFD and delay-line behavior

The measured time difference between the input and output pulses of the first-order delay circuit increased linearly with increasing resistor value (R_d) with almost the same slope as the calculated delay. However, the measured delay had a bias of ~ 0.39 ns relative to the calculated values, as shown in figure 7. This bias is most likely due to the routing delay in the PCB and the propagation delay of the op-amp.

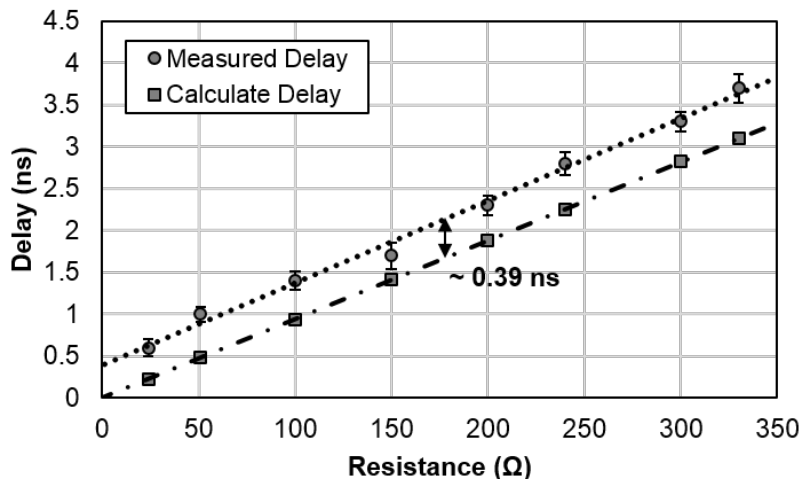


Figure 7. Measured delay (circle) and calculated delay (square) dependencies on the delay resistor (R_d).

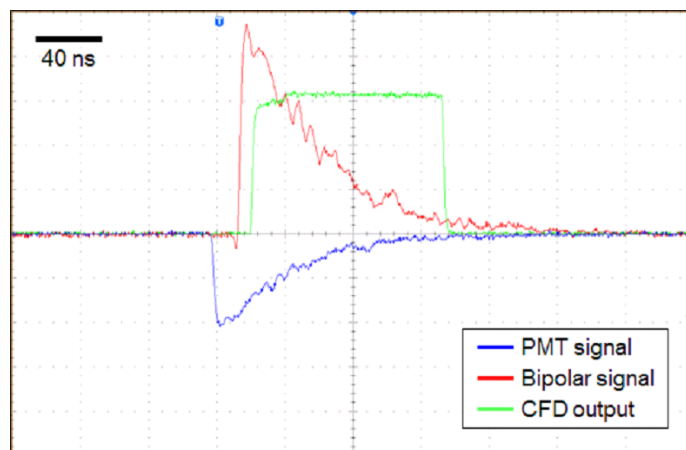


Figure 8. PMT signal (blue), generated bipolar signal (red), and output signal (green) captured using the MSO4034 oscilloscope. The delay and threshold were set to 2.9 ns and 50 mV, respectively. The voltage scale was changed channel by channel to obtain a clear pulse shape.

The behavior of the NDL CFD with a measured delay of 2.9 ns and a threshold of 50 mV is shown in figure 8. The signal propagation delay can be found from the generated bipolar signal and the digital CFD output. The latency of the developed NDL CFD was ~ 20 ns.

3.3 Timing measurement of the TOF detector

Figure 9 presents the CRT of the LYSO-PMT detector as measured using the NDL CFD and the DL CFD. The CFDs with 20% attenuation generally yielded better results (i.e., lower CRT) than those with 40% attenuation. The results from the NDL CFD and the DL CFD show almost the same pattern with increasing delay; however, at small delays, the DL CFD yielded slight but not significantly better CRTs. The best CRTs were 309.3 ± 14.3 and 301.6 ± 6.6 ps, which were measured for a 1.4 ns delay with the NDL CFD and a 1.0 ns delay with the DL CFD, respectively, as shown in figure 10. This time performance degradation includes not only the electrical noise and

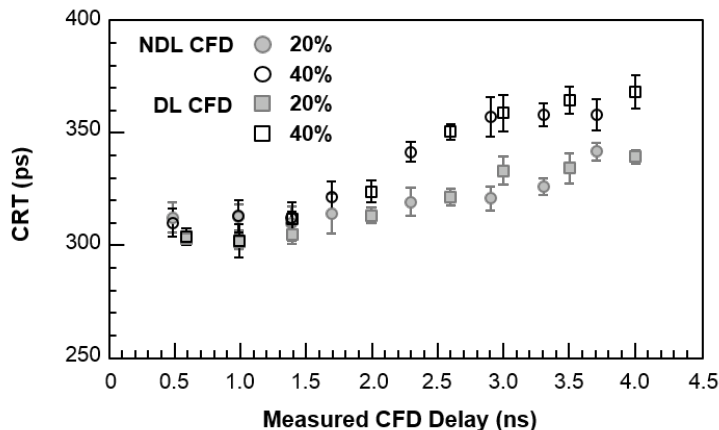


Figure 9. CRTs with 20 and 40% attenuation relative to various CFD delays. Circles denote the NDL CFD and squares denote the conventional DL CFD. Filled symbols denote the 20% CFD fraction while open symbols denote the 40% CFD fraction.

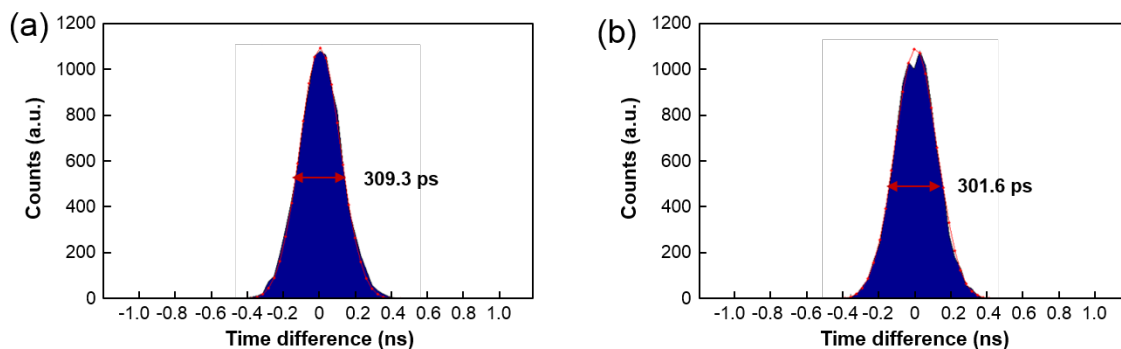


Figure 10. Timing difference spectra at the TDC obtained using (a) the active delay method and (b) the transmission line method with the PMT signal in optimal condition.

the non-zero offset voltage of the delay circuit, but also includes the non-linearity of the TDC. The noise and the non-zero offset voltage caused by the non-ideal properties of the op-amp may lead to a trigger time shift at the zero-crossing detector.

The energy resolution was unaffected by the timing discrimination setup and the measured energy resolution was $\sim 10\%$.

4 Discussion

This study developed a NDL CFD based on the Padé approximant and verified its suitability for TOF PET applications with a CRT of around 300 ps. The experimental results demonstrate that the behavior of the developed NDL CFD is similar to that of a conventional DL CFD and that it yields a reasonable timing performance for a TOF-PET. The proposed method also provides higher spatial efficiency than the traditional CFD by removing the large amount of space required for the long delay line. It is also easy to control the delay time with small time intervals by simply changing the resistance in the delay circuit. This makes it possible to determine the appropriate experimental setup accurately.

While the second-order approximant is better than the first-order approximant in terms of bandwidth and time domain ripple, implementation of the second-order approximant requires one additional op-amp stage, which adds an op-amp propagation delay and a routing delay.

One minor disadvantage of the NDL CFD is the bandwidth dependence on the delay value. However, recent studies have shown that the optimal CFD delay required for the novel PMT and SiPM detector to obtain the best possible time resolution is less than 2 ns [22, 25]. In the simulation study described in this paper, we demonstrate that the first-order delay circuit performs sufficiently for small delay. Another disadvantage is the output offset voltage level variation in the delay circuit caused by the non-zero bias current and the non-zero input offset voltage, which may introduce offsets to the zero-crossing detector. This effect can be minimized to carefully match the equivalent impedance of both the non-inverting and inverting inputs of the op-amp. In this study, we optimized the impedance of the inverting input (i.e., R_1 in figure 1(a)) to a 1.5 ns delay, and little degradation was found for delays of less than 1 ns.

Despite these disadvantages, the experimental results show that it may be possible to use a NDL CFD with a fast scintillation detector for a modern TOF PET. To generate a 5 ns delay with a conventional transmission line, a very long length of ~ 1 m is needed. This would also require carefully considered impedance matching for the connection between the transmission line and the PCB for the transmission line to minimize distortion. The proposed NDL CFD would be advantageous for high-density systems with high count rates.

5 Conclusion

We developed a CFD using an active delay and compared its performance with that of a CFD using transmission delay. The active delay provides a reasonable time performance, high spatial efficiency, and flexible delay control. Use of a NDL CFD allows the entire system to be compact but provides timing performance comparable to that of a CFD with a transmission line.

Acknowledgments

This work was supported by grants from the National Research Foundation of Korea (NRF) funded by the Korean Ministry of Science, ICT and Future Planning (grant no. NRF-2014M3C7034000), and the Korea Health Technology R&D Project through the Korea Health Industry Development Institute (KHIDI), funded by the Ministry of Health & Welfare, Republic of Korea (grant no. HI14C1135).

References

- [1] S. Junnarkar, *Time-to-digital converter circuits in radiation detection systems*, in *Electronics for Radiation Detection*, K. Iniewski ed., CRC Press LLC (2010), pg. 337.
- [2] W. Maichen, *Digital Timing Measurements: From Scopes and Probes to Timing and Jitter*, Springer, *Frontiers in Electronic Testing* **33** (2006) 1.
- [3] LHCb collaboration, *The LHCb Detector at the LHC*, 2008 *JINST* **3** S08005.
- [4] I.V. Chernushevich, A.V. Loboda, and B.A. Thomson, *An introduction to quadrupole-time-of-flight mass spectrometry*, *J. Mass. Spectrom.* **36** (2001) 849.

- [5] M. Conti, *Focus on time-of-flight PET: the benefits of improved time resolution*, *Eur. J. Nucl. Med. Mol. Imag.* **38** (2011) 1147.
- [6] C.L. Kim, G.-C. Wang and S. Dolinsky, *Multi-pixel photon counters for TOF PET detector and its challenges*, *IEEE Trans. Nucl. Sci.* **56** (2009) 2580.
- [7] W.-S. Choong, *Investigation of a multi-anode microchannel plate PMT for time-of-flight PET*, *IEEE Trans. Nucl. Sci.* **57** (2010) 2417.
- [8] D.R. Scharrt et al., *LaBr₃: Ce and SiPMs for time-of-flight PET: achieving 100 ps coincidence resolving time*, *Phys. Med. Biol.* **55** (2010) N179.
- [9] M. Conti, *Improving time resolution in time-of-flight PET*, *Nucl. Instrum. Meth. A* **648** (2011) S194.
- [10] J.S. Lee and J.H. Kim, *Recent advances in hybrid molecular imaging systems*, *Semin. Musculoskelet. Radiol.* **18** (2014) 103.
- [11] T.J. Paulus, *Timing electronics and fast timing methods with scintillation detectors*, *IEEE Trans. Nucl. Sci.* **32** (1985) 1242.
- [12] W.R. Leo, *Techniques for Nuclear and Particle Physics Experiments: A How-to Approach*, Springer-Verlag, Berlin Heidelberg (1987).
- [13] R. Vinke et al., *Optimizing the timing resolution of SiPM sensors for use in TOF-PET detectors*, *Nucl. Instrum. Meth. A* **610** (2009) 188.
- [14] S.I. Kwon, and J.S. Lee, *Signal encoding method for a time-of-flight PET detector using a silicon photomultiplier array*, *Nucl. Instrum. Meth. A* **761** (2014) 39.
- [15] D. Gedcke and W. McDonald, *A constant fraction of pulse height trigger for optimum time resolution*, *Nucl. Instrum. Meth.* **55** (1967) 377.
- [16] R. Nutt, D. Gedcke and C. Williams, *A comparison of constant fraction and leading edge timing with NaI(Tl) scintillators*, *IEEE Trans. Nucl. Sci.* **17** (1970) 299.
- [17] B. Turko and R. Smith, *A precision timing discriminator for high density detector systems*, *IEEE Trans. Nucl. Sci.* **39** (1992) 1311.
- [18] D.M. Binkley, *Performance of non-delay-line constant-fraction discriminator timing circuits*, *IEEE Trans. Nucl. Sci.* **41** (1994) 1169.
- [19] G.A Baker Jr. and P. Graves-Morris, *Padé Approximants*, Cambridge University Press, New York, U.S.A. (1996).
- [20] L. Zhou, A. Safarian and P. Heydari, *CMOS wideband analogue delay stage*, *Electron. Lett.* **42** (2006) 1213.
- [21] J. Lam, *Convergence of a class of Padé approximations for delay systems*, *Int. J. Contr.* **52** (1990) 989.
- [22] M. Ito, J.P. Lee and J.S. Lee, *Timing performance study of new fast PMTs with LYSO for time-of-flight PET*, *IEEE Trans. Nucl. Sci.* **60** (2013) 30.
- [23] J.P. Lee, M. Ito and J.S. Lee, *Evaluation of a fast photomultiplier tube for time-of-flight PET*, *Biomed. Eng. Lett.* **1** (2011) 174.
- [24] A. Kuhn et al., *Design of a lanthanum bromide detector for time-of-flight*, *IEEE Trans. Nucl. Sci.* **51** (2004) 2550.
- [25] T. Szczesniak et al., *Time resolution of scintillation detectors based on SiPM in comparison to photomultipliers*, *IEEE Nucl. Sci. Symp. Conf. Rec.* **1** (2010) 1728.